ARL-CR-0848 • MAY 2020

DEVCOM ARMY RESEARCH LABORATORY

Unmanned Vertical Take-off and Landing (VTOL) Propulsion: Scalability of Quadcopter Rotor–Motor Configurations outside the Small Unmanned Aerial System (sUAS) Regime

by Kendy Edmonds and D Blake Stringer

under contract W911NF-18-2-0024

NOTICES

Disclaimers

The findings in this report are not to be construed as an official Department of the Army position unless so designated by other authorized documents.

Citation of manufacturer's or trade names does not constitute an official endorsement or approval of the use thereof.

Destroy this report when it is no longer needed. Do not return it to the originator.

ARL-CR-0848 ● MAY 2020

Unmanned Vertical Take-off and Landing (VTOL) Propulsion: Scalability of Quadcopter Rotor–Motor Configurations outside the Small Unmanned Aerial System (sUAS) Regime

Kendy Edmonds and D Blake Stringer
Kent State University

under contract W911NF-18-2-0024

REPORT DOCUMENTATION PAGE

Form Approved
OMB No. 0704-0188

1. REPORT DATE *(DD-MM-YYYY)*	2. REPORT TYPE	3. DATES COVERED (From - To)
May 2020	Contractor Report	6 June 2019

4. TITLE AND SUBTITLE
Unmanned Vertical Take-off and Landing (VTOL) Propulsion: Scalability of Quadcopter Rotor–Motor Configurations Outside the Small UAS (sUAS) Regime

5a. CONTRACT NUMBER
W911NF-18-2-0024

5b. GRANT NUMBER

5c. PROGRAM ELEMENT NUMBER

6. AUTHOR(S)
Kendy Edmonds and D Blake Stringer

5d. PROJECT NUMBER

5e. TASK NUMBER

5f. WORK UNIT NUMBER

7. PERFORMING ORGANIZATION NAME(S) AND ADDRESS(ES)
Kent State University
800 E Summit St.
Kent, OH 44240

8. PERFORMING ORGANIZATION REPORT NUMBER

9. SPONSORING/MONITORING AGENCY NAME(S) AND ADDRESS(ES)
CCDC Army Research Laboratory
ATTN: FCDD-RLV-P
NASA Glenn Research Center
21000 Brookpark Road, Mail Stop 23-3
Cleveland, OH 44135

10. SPONSOR/MONITOR'S ACRONYM(S)

11. SPONSOR/MONITOR'S REPORT NUMBER(S)
ARL-CR-0848

12. DISTRIBUTION/AVAILABILITY STATEMENT
Approved for public release; distribution is unlimited.

13. SUPPLEMENTARY NOTES
ORCID ID: Kendy Edmonds, 0000-0002-4375-2638

14. ABSTRACT

Consumer-based small unmanned aircraft systems (sUASs) or "drone" products with a useful load less than 55 lbf use variable-speed rotor–motor configurations to provide aircraft thrust and maneuverability. The success of these quadcopter-type platforms makes them desirable to scale into larger UAS groups. However, the feasibility of these variable-speed configurations is unknown in the commercial/military UAS design space between 100 and 1,000 lbf of useful load. As the size of the rotor–motor configurations increases, so does their inertia. It is unclear what the effects of increased inertia are on the transient settling time of the rotor–motor system. A vertical-take-off-and-landing propulsion experiment stand was constructed to characterize the transient performance of various configurations. Inertia has an effect on transient coast-down settling time of a rotor–motor. However, inertia is not the only contributor to the settling time. A stochastic model was generated from the experimental data to predict coast-down settling time as a function of significant parameters. Temperature and thermal management proved to be significant items and must be addressed when using electrical motors for large rotary-wing applications. While the results presented are significant, more-expansive experiments are required to adequately predict the transient response of larger systems.

15. SUBJECT TERMS
rotorcraft, propulsion, rotor, motor, inertia, transient, drone, quadcopter, scaling

16. SECURITY CLASSIFICATION OF:			17. LIMITATION OF ABSTRACT	18. NUMBER OF PAGES	19a. NAME OF RESPONSIBLE PERSON
a. REPORT	b. ABSTRACT	c. THIS PAGE			Mark R Riggs
Unclassified	Unclassified	Unclassified	UU	46	19b. TELEPHONE NUMBER (Include area code) 410-278-9604

Standard Form 298 (Rev. 8/98)
Prescribed by ANSI Std. Z39.18

Contents

List of Figures

List of Tables

Summary

Consumer-based small unmanned aircraft systems (sUASs) or “drone” products with a useful load less than 55 lbf use variable-speed rotor–motor configurations to provide aircraft thrust and maneuverability. The success of these quadcopter-type platforms makes them desirable to scale into higher UAS groups. However, the feasibility of these variable-speed configurations is unknown in the commercial/military UAS design space between 100 and 1,000 lbf of useful load.

As the size of the rotor–motor configurations increases, so does their inertia. It is unclear what the effects of the increased inertia are on the transient settling time of the rotor–motor system. To that end, a vertical-take-off-and-landing (VTOL) propulsion experimental test stand was constructed at Kent State University to characterize the transient performance of various configurations. Experiments captured over 35 parameters of seven different rotor–motor combinations and yielded approximately 4,800 data points.

It was discovered that inertia does indeed have an effect on the transient coast-down settling time of a rotor–motor. However, the inertia is not the only contributor to the settling time. A stochastic model was generated from the experimental data to predict coast-down settling time as a function of significant parameters. Temperature and thermal management proved to be significant items of concern and must be addressed when using electrical motors for large rotary-wing applications. While the results presented are significant, more-expansive experiments are required to adequately predict the transient response of much larger systems.

1. Introduction

The rapid proliferation of quadcopter and other vertical-take-off-and-landing (VTOL) configurations in the consumer market over the past decade has helped create a global "drone" market worth $14 billion in 2018 and projected to triple to $43 billion by 2024.[1] In addition, the US Federal Aviation Administration released regulatory guidance on the remote pilot requirements for legal commercial operation of small unmanned aircraft systems (sUASs),[2] which are commensurate with the requirements of other nations.[1] At the same time, however, these VTOL configurations exposed some significant disadvantages, specifically the problems of power and endurance.[3–5]

Nevertheless, sUAS VTOL configurations have proven their feasibility as a platform for several applications to include logistics and payload delivery.[3,4] In fact, the latest drone market report[1] predicts the greatest expected growth in the drone delivery sector, with transportation and warehousing taking over as the fastest-growing UAS industry sector.

The potential then exists to design and build military platforms that carry greater payloads with higher range and endurance capabilities, especially in challenging terrain and operating conditions. Considering the US Department of Defense's projected expenditures of approximately $4.6 billion in unmanned systems procurement, research, and development in FY2020 budget,[6] along with the commercialized drone activities of corporations such as Amazon and United Parcel Service,[3,7] it is therefore critical to determine the scalability of current sUAS propulsion methods to support these larger platforms and overcome the disadvantages of power and endurance.

One consideration in scaling is the transient behavior of the rotor–motor system. Conventional sUAS platforms are propelled by electric fixed-pitch variable-speed motors, while traditional rotorcraft are powered using variable-pitch constant-speed rotor systems. As the platform increases in size, so too do the rotors and electric motors, leading to an increase in the rotational inertia of the propulsion system. From an intuitive perspective, the increased inertia means that the larger systems do not respond as quickly as smaller rotors,[8] possibly affecting the suitability of variable-speed motors at larger scales.

The objective of this research effort has been to experimentally measure and quantify the transient response of variable-speed rotor–motor configurations through the following research activities:

- Construction of a table-top experimental rotor–motor static test stand

- Demonstration of data-extraction capabilities
- Performance characterization of varying-size rotor and disk diameters
- Determination of static test-bench scalability

In pursuing that objective, the investigators made other discoveries regarding the nature of unmanned VTOL propulsion:

- The investigators measured the transient response of seven different rotor–motor combinations.
- Based upon the initial results, the investigators expanded the initial experimental test matrix to capture a wide array of input variables. This resulted in a model for predicting the transient times using variable input factors such as rotor and motor inertia, throttle setting, and so on.
- The investigators observed and recorded thermal characteristics of the rotor–motor combinations. In some cases, the experiments resulted in a thermal runaway and motor damage.

2. Background

For purposes of this research, it was assumed that the unmanned VTOL platform scales in size to operate within the Group III UAS regime: a maximum gross takeoff weight of 1,320 lbf, maximum operating altitude of 18,000 ft mean sea level (MSL), and no airspeed restrictions. This roughly corresponds to an aircraft with a maximum payload of 400 lbf and a range radius of 50–1,000 nmi.[9] However, this is not the upper limit of the applications of this study. The platform could easily cross the threshold into the Group IV UAS category: greater than 1,320 lbf and below 18,000 ft MSL. In addition, the feasibility of large variable-speed rotor–motors could also be applied to urban air-transport development aircraft, or "sky taxis," such as those advocated by Uber Elevate.[10]

2.1 Scaling Ideal Hover-Power Requirements

Quadcopter-type power requirements increase drastically as size increases, as illustrated in Fig. 1. The figure displays two contour plots for the variation of hover-power requirements of a quadcopter as a function of weight and disk loading. The triangular data point represents the location of a familiar sUAS in this regime, the Phantom 3 Professional, offered by DJI. The inverted triangle represents the Robinson R-22 helicopter, which has a similar payload capacity to the nominal UAS platform and is represented by the circle. This nominal aircraft assumes four 36-inch-diameter rotors and a 1,000-lbf gross weight. The comparison of these

three platforms is presented in Table 1. Note that the disk loading of the Group III UAS is substantially higher than the DJI or R-22.

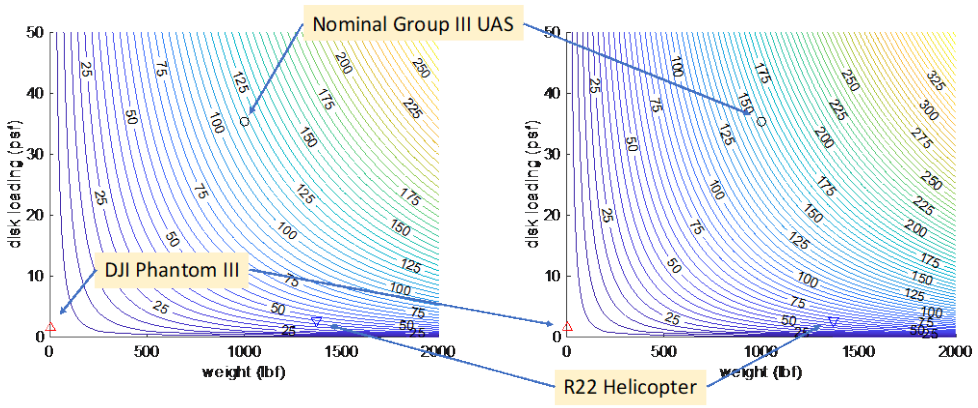

Fig. 1 Ideal hover-power contours vs. weight and disk-loading in (left) horsepower and (right) kilowatts

Table 1 Platform ideal hover-power comparison

Platform	Disk loading (thrust/area)	Gross weight (W)	Ideal hover power (P)		Maneuver power (P_m)	
	psf	lbf	hp	kw	hp	kw
DJI Phantom III	1.6	2.82	0.094	0.07	0.266	0.199
R-22 Helicopter	2.57	1,370	60	45	170	127
Group III UAS	35.4	1,000	157	117	444	331

The hover-power requirements do not include any transient power requirements for maneuvering the aircraft, especially abrupt maneuvering. Conventional sUAS design calculations generally assume doubling the thrust to ensure adequate power.[11] This technique essentially models a 2-g maneuver. Using this rule of thumb for the nominal platform results in a transient power requirement of 444 hp (331 kW). This is a 283% increase over its ideal hover-power requirement in Table 1.

Important items in this analysis are the following: 1) As the size of the aircraft grows, increasing rotor diameter assists in maintaining manageable power requirements. 2) As the size of the rotors increases, so do the profile power requirements for spinning the rotors to overcome inertia and blade profile drag. These increased power requirements are in addition to the ideal hover-power requirements presented in Table 1.

2.2 The State of the Art in 2019

The literature has not yielded much information on current or previous studies on the scalability of variable-speed rotors, indicating this is a relatively untouched focus area of rotary-wing propulsion. Indeed, as presented in Davis,[12] the focus on scalability and rotor inertia "seems to present a gap" in the current state of the art. Much of the current research discussing rotor inertia in quadcopter applications use the inertia as a parameter for determining other parameters.[13–18] Some authors do provide data on the impacts of rotor inertia and its importance to maneuvering characteristics.[19–21] However, these discussions still fall within the very low end of the sUAS regime. By and large, many discussions of transients in the literature focus on the stability and control of the sUAS during transient periods.[13–18,22–28]

Some transient studies in the literature have focused on fault detection in motors and shafts.[29,30] The limited nature of material directly applicable in this area may be due to the current focus of quadcopter dynamics in the sUAS regime, where rotor transient impacts are somewhat minimal, except for racing or conditions requiring extreme agility.[8]

2.3 Kent State University VTOL UAS Propulsion Research to Date

VTOL research at Kent State University began in 2015. It grew out of an unfunded benchtop construction stand for a student research project.[12] The purpose of this previous work was to experimentally measure and quantify the transient response of variable-speed rotor–motor configurations through 1) construction of a tabletop experimental rotor–motor static test stand, 2) demonstration of data extraction capabilities, 3) performance characterization of varying-size rotor and disk diameters, and 4) determination of static test bench scalability.

An image of the initial test stand and some of the data results are presented in Fig. 2.

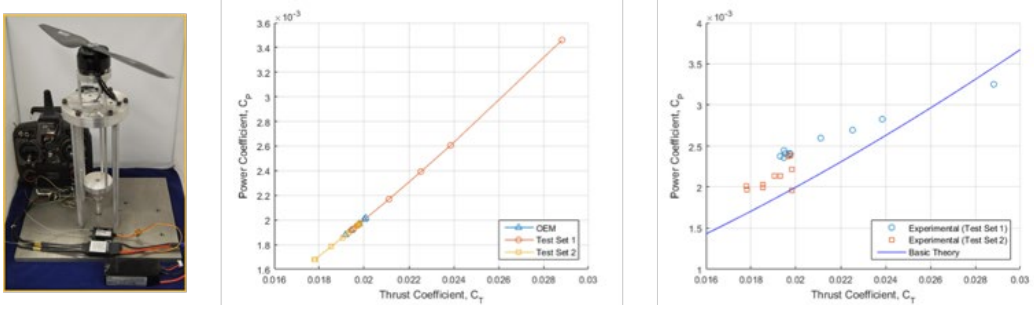

Fig. 2 Initial test stand and research results at Kent State University

The primary discoveries of this initial research resulted in 1) the proof of concept, 2) a validation of the data-acquisition capabilities based on a comparison of experimental data and rotor–motor data supplied by the original equipment manufacturer, and 3) a set of design recommendations for scaling to a larger-thrust experimental test stand.[12,31] However, the transient response was never fully investigated in that earlier study.

There are three questions for scaling quadcopter-type applications using variable-speed motors:

1) At what size rotor–motor system does the inertia noticeably affect the transient time between different motor speeds?

2) Based upon the results from No. 1, what is the maximum rotor diameter that can effectively use variable-speed motors?

3) How do these transient conditions affect and determine maneuverability? The purpose, products, and military payoff of this research are presented in Fig. 3.

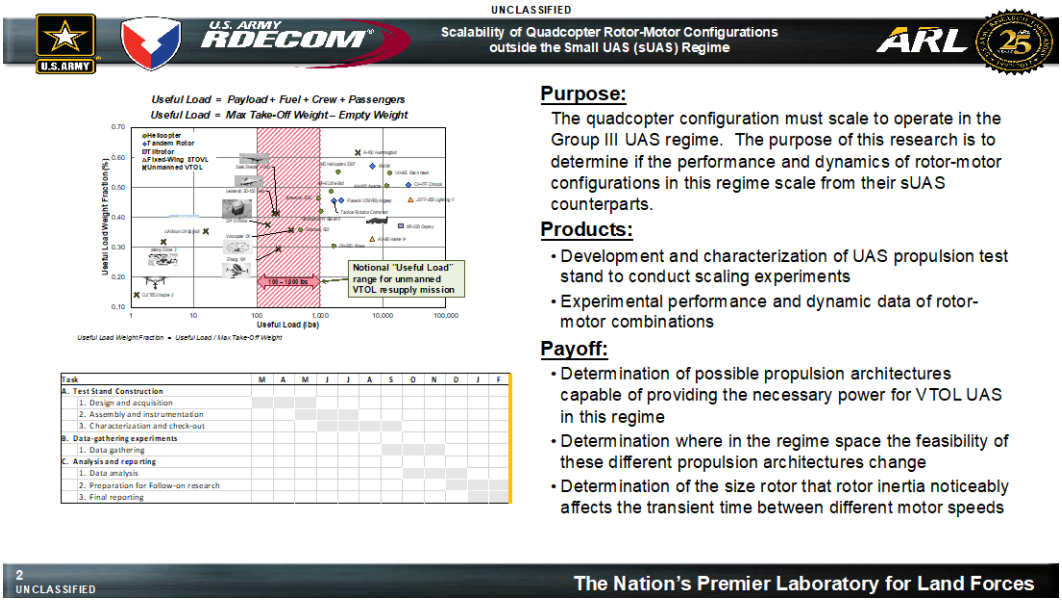

Fig. 3 Purpose, products, and payoff assessment

3. Experimental Apparatus, Equipment, and Test Matrix

3.1 Experimental Test Bench Description

Kent State University's Unmanned VTOL Propulsion Experimental Test Stand was designed and built for this study. It is a commercial-off-the-shelf system: the Series 1780 Thrust Stand and Dynamometer v1, manufactured by RC Benchmark,[32] depicted in Fig. 4. The image on the left provides a sterile image of the stand. The image on the right illustrates the placement and identification of the components. The stand is encased in a 60- × 60-inch plywood shroud and frame. Three 1/4-inch-thick × 14-inch-wide steel plates surround the tip-path-plane area of the shroud to provide ballistic protection from the rotor.

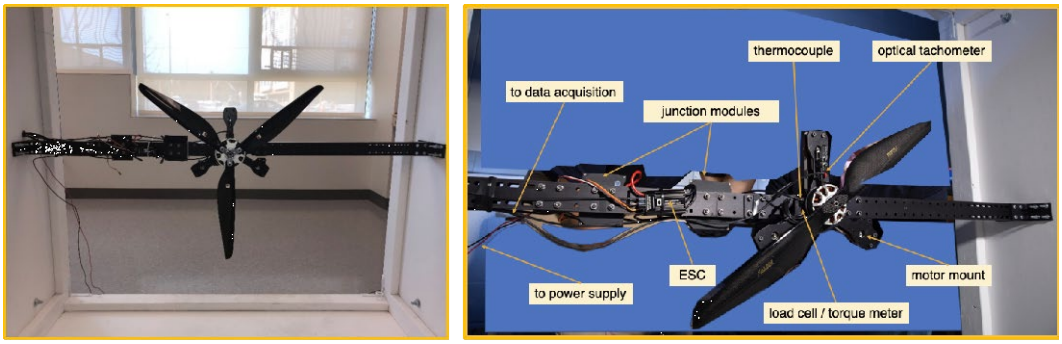

Fig. 4 Kent State University VTOL Propulsion Test Stand

The static thrust stand records the following data: time, electronic speed controller (ESC) setting, pulse-width modulation (pwm), motor optical speed (rpm), thrust, torque, electrical power in, mechanical power out, temperature of desired components, transient response time, maximum acceleration, and system efficiency estimations. The operational limits of the stand are provided in Table 2.

Table 2 VTOL Propulsion Test Stand limits

Threshold	Voltage (V)	Current (A)	Speed (rpm)	Thrust (lbf)	Torque (ft.lbf)	Power (kW)
Maximum	60	100	190,000	±44	±7.39	6

Software control of the test stand occurs via software developed by RC Benchmark. The software allows both manual control of the motor and automated testing and data recording. Details outlining the specific experiments used for this study are addressed in later sections.

Voltage input to the bench was regulated by using 12-V automotive batteries connected in series with a minimum configuration of one battery and a maximum

configuration of five. This method of power management was adequate for the tests required for this study. The stand contains two junction boxes that allow the operator to quickly switch between power sources, ESCs, and electric motors.

3.2 Rotor–Motor Configurations

This study used four different rotors in testing and they are presented from lightest to heaviest in Table 3. The fourth rotor is a left-turning TM 15 × 5, two-blade article, which has the same parameters as its right-turning counterpart in Table 3. The rotor designation 15 × 5 indicates a 15-inch diameter with a 5-inch pitch. Both the international (SI) and UK systems of measurement are presented.

Table 3 sUAS rotor properties

Rotor	Mass		Weight	Diameter		Disk area	Inertia	Mean chord	Solidity
	g	slug	lbf	inches	ft	ft^2	$slug.ft^2$	inches	d'less
TM-Rotor 15 × 5R, 2-blade TM 15.5	28.1	0.00192	0.06193	15	1.25	1.227	2.24E-04	1.01	0.0857
Falcon Rotor 27 × 8.8R, 2-blade Falcon 27	98	0.00671	0.21618	27	2.25	3.976	0.0025	1.79	0.0844
KDE Rotor 30.5 × 9.7L, 3-blade KDE 30.5	222.5	0.0152	0.491	30.5	2.54	5.074	0.0064	1.9	0.119

Notes: slug = unit of mass; d'less = dimensionless.

Five electric motors were used in the study and are presented from lightest to heaviest in Table 4.

Table 4 Motor properties

Motor	Mass		Weight	Diameter		Inertia	Motor kV
	g	slug	lbf	mm	ft	$slug.ft^2$	rpm/V
KDE 4215XF-465 Mini	218	0.015	0.482	48.3	0.1583	0.000047	465
KDE 7215XF-135 KDE	555	0.038	1.2245	80.8	0.2651	0.000334	135
T-Motor P80-120 P80	565	0.0387	1.2466	91.6	0.3005	0.000437	120
KDE 10218XF-105 Mega	1075	0.0737	2.3718	109.1	0.358	0.00118	105
Turnigy Rotomax 150 cc Turnigy	2530	0.1734	5.5821	109	0.3576	0.002771	150

These combined for a total of seven rotor–motor configurations. Table 5 presents the parameters of each different configuration. The inertia values in Table 5 capture the sum of the inertias of the rotating part of the motor (stator) and the rotor. For purposes of this project, the total configuration inertias assume only 20% of the motor mass is rotating.

Table 5 Rotor–motor configurations

Motor	Mass		Weight	Inertia	Inertia
	g	slug	lbf	slug.ft^2	kg.m^2
Mini TM 15.5	246.5	0.0169	0.5439	2.34E-04	3.17E-04
P80 Falcon 27	663	0.0454	1.4628	2.58E-03	3.50E-03
KDE 30.5	777.5	0.0533	1.7155	6.49E-03	8.80E-03
P80 KDE 30.5	787.5	0.054	1.7376	6.51E-03	8.83E-03
Mega Falcon-27	1173	0.0804	2.588	2.73E-03	3.70E-03
Mega KDE 30.5	1297.5	0.0889	2.8628	6.66E-03	9.03E-03
Turnigy KDE 30.5	2752.5	0.1886	6.073	6.98E-03	9.46E-03

The mass and inertia for each rotor–motor configuration are presented in Figs. 5 and 6, respectively. In Fig. 5, the chart on the left shows the total weight of each configuration with the rotor and motor contributions to the total weight displayed for each. The chart on the right in Fig. 5 displays the rotor and motor contributions to weight as percentages of the whole. Figure 6 presents the inertia of the rotor–motor configurations in the same manner as Fig. 5.

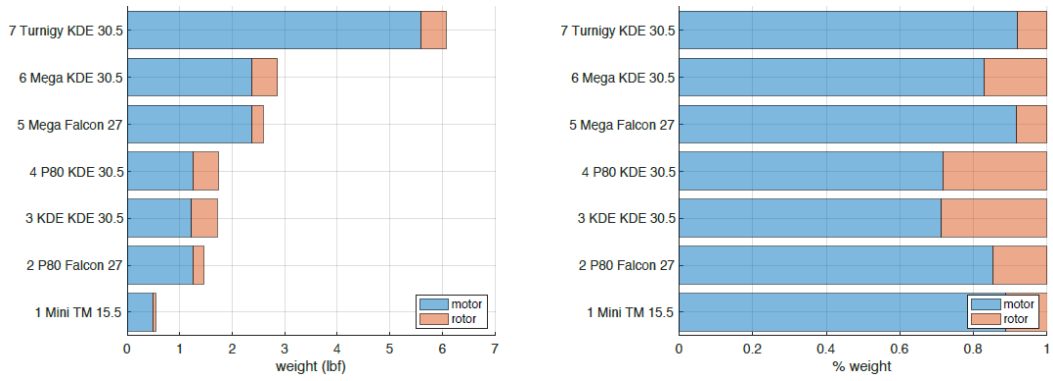

Fig. 5 Contribution of rotor and motor to total mass/weight

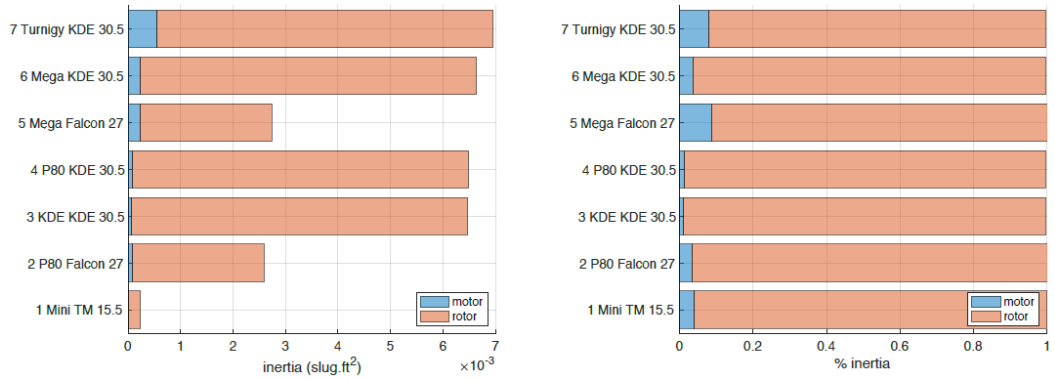

Fig. 6 Contribution of rotor and motor to total inertia

These charts illustrate that the motor provides a majority of the mass of the rotor–motor system. For these seven configurations the average contribution of the motor mass to the total mass is 83%, with the rotor providing only 17% of the mass. However, as seen in Fig. 6, the rotor provides an overwhelming majority of the total inertia of the system. For inertia, the rotor contributes on average 96% of the total rotor–motor inertia. Note this contribution assessment assumes only 20% of the motor mass is actually rotating and, therefore, only 20% of the motor inertia contributes to the system.

Figure 7 shows the motors used in this study with their shortened designations below. The Mini on the far right is not the actual motor used in the study. The actual motor looks like the Mega and KDE motors, but is the approximate diameter of the motor pictured on the far right.

Fig. 7 Motor comparison

The electronic speed controller (ESC) used with the Turnigy, Mega, P80, and KDE configurations was the KDE-UAS125UVC. The ESC used with the Mini was the

KDE XF-UAS75HVC. All manufacturer default settings remained the same for both controllers.

3.3 Test-Stand Characterization

A series of initial experiments was conducted to characterize and validate the thrust stand. Manufacturers of larger electric motors often provide a performance datasheet outlining the various parameters at a variety of power settings, such as rotational speed, thrust, and motor efficiency. These were used to compare with experimental data recorded from the static thrust stand to verify proper installation of motors and instrumentation each time a new motor was placed on the stand. An example of these characterization data for the P80 motor is presented in in Fig. 8.

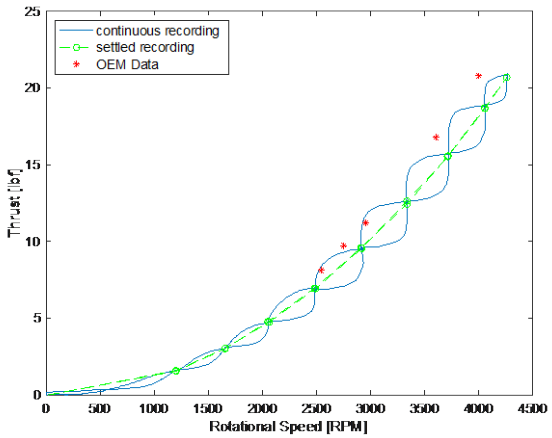

Fig. 8 P80 full power thrust curve (48-V input)

As mentioned, the thrust bench is capable of running a diverse set of automated experiments. The software comes with a variety of preconfigured scripts that can be tailored to specific applications. The main differences between the scripts are the ways in which the user controls an experiment. For example, in the preconfigured Continuous Sweep script, the user can select the starting and ending throttle setting (indicated by ESC pwm), the time the motor takes to ramp up from the starting throttle to the ending throttle, how long the motor will stay running at the higher throttle setting, and whether the script coasts the motor back down to the starting throttle or not.

In contrast, with the built-in Settling Time script, the user controls the steps the motor will take in terms of throttle percentage. This script will automatically progress to the next step once the system determines the motor is “settled” and the user cannot control how long it will stay on one throttle-percentage input. Variations of the Settling Time script were used for the majority of this study and will be expanded on further.

Some preconfigured automated scripts, such as the Settling Time script, have the option to record continuously (at approximately 4 data points per second) or to strictly return one point after the script has determined the system is settled. In Fig. 8 the dashed line is an example of a "settled recording" script, where one point is recorded after the system has settled. The point that is recorded is indicated by the circle. The solid line is an example of a "continuous recording" script, which allows for a visualization of how the rotor(s) ramp up and coast down. For each experiment, both settled and continuous-recording scripts were run for consistency.

3.4 Experimental Test Matrix

There were three different transient response experiments based upon throttle setting: 1) ramping up from 50% throttle to 75% throttle and coasting back down to 50% throttle, 2) ramping up from 50% throttle to 90% throttle and coasting back down to 50% throttle, and 3) ramping up from 10% throttle to 90% throttle and coasting back down to 10% throttle. These represent 1) low, 2) medium, and 3) high throttle differentiations, respectively. These experiments were chosen to capture both drastic changes in motor speed as well as subtle changes more representative of rotational speed changes required for basic maneuvering.

Measuring the transient response used variations of the Settling Time script. The control script conducted a series of checks to ensure the motor was stabilized before moving on to the next step. The script first took a series of 30 consecutive rotational-speed data points, examined them to see if the series contained both increasing and decreasing values, and verified that the motor was within ±5 rpm. Once this parameter was met, the software proceeded to the next throttle setting. As mentioned, the script had the option to record all parameter values at a constant rate or to strictly record a single set of all parameter values after the system was deemed to be settled. Both data recording methods were used.

Each experiment executed 10 sequences of a ramp-up followed by a coast-down between the minimum and maximum throttle settings described at the beginning of this section. This resulted in 20 settling-time data points per experiment. To ensure repeatability, each experiment was conducted three times.

Using this methodology resulted in 18 total experiments for each rotor–motor configuration per voltage setting. Most of the rotor–motor configurations were run using one to five 12-V automotive batteries (nominally 12–60 V). Ideally, this resulted in 90 total experiments per rotor–motor configuration. With 10 data points per experiment, this resulted in 900 total data points per rotor–motor configuration. In reality, some of the motors behaved differently under higher power conditions or had operating limits lower than the test matrix, so the test matrix had to be

altered. Nevertheless, approximately 4,860 transient data points were collected during this study.

The entire test matrix is presented in Table 6 and shows the number of experiments for each setting. Exceptions to the test procedure described previously are further clarified.

Table 6 Experimental test matrix

No. batteries	1	2	3	4	5	Total
Throttle			**Mini/TM 15.5[a]**			
10%–90%	6	6	0	0	0	12
50%–75%	6	6	0	0	0	12
50%–90%	6	6	0	0	0	12
			P80/Falcon 27			
10%–90%	6	6	6	6	6	30
50%–75%	6	6	6	6	6	30
50%–90%	6	6	6	6	6	30
			KDE/KDE 30.5[b]			
10%–90%	0	0	0	0	0	0
50%–75%	6	6	6	0	0	18
50%–90%	6	6	0	0	0	12
			P80/KDE 30.5			
10%–90%	6	6	6	6	6	30
50%–75%	6	6	6	6	6	30
50%–90%	6	6	6	6	6	30
			Mega/Falcon 27[c]			
0%–90%[c]	0	0	0	0	2	2
10%–90%	6	6	6	6	0	24
50%–75%	6	6	6	6	4	28
50%–90%	6	6	6	6	2	26
			Mega/KDE 30.5[c]			
0%–90%[c]	0	0	0	0	2	2
10%–90%	6	6	6	6	2	26
50%–75%	6	6	6	6	4	28
50%–90%	6	6	6	6	2	26
			Turnigy/KDE 30.5[c]			
0%–90%[c]	0	0	0	6	0	6
10%–90%	6	6	6	6	0	24
50%–75%	6	6	6	6	0	24
50%–90%	6	6	6	6	0	24

[a] The KDE Mini was limited by voltage capability, which limited its test matrix.

[b] The KDE motor(s) used resulted in thermal runaway conditions twice despite operating well within normal limits. Two motors were used, and both experienced runaway conditions, which significantly reduced the test matrix for this configuration.

[c] The larger motors behaved differently at the highest voltage settings. Due to these effects, a throttle setting of 0%–90% was also incorporated. The Turnigy motor significantly drained the battery at 60 V. Therefore, all experiments at 60 V were omitted. The Turnigy motor vibrated the mast significantly at some of the lower throttle settings, although data were extracted.

The parameters measured included input voltage (V), current (I), settling time (Δt), maximum acceleration (a_{max}), electrical power in (P_{in}), mechanical power out (P_{out}), mechanical efficiency (η), thrust (T), torque (Q), rotational speed (Ω), and temperature (both motor and ESC).

3.5 Rotary-Wing Aerodynamic Calculations

All rotary-wing calculations using thrust, power, and torque data assume the aircraft to be at a stationary hover. For simplicity, all analysis used the equations associated with basic momentum theory, which is pictured in Fig. 9. The pertinent equations used in this analysis are provided in the Appendix.

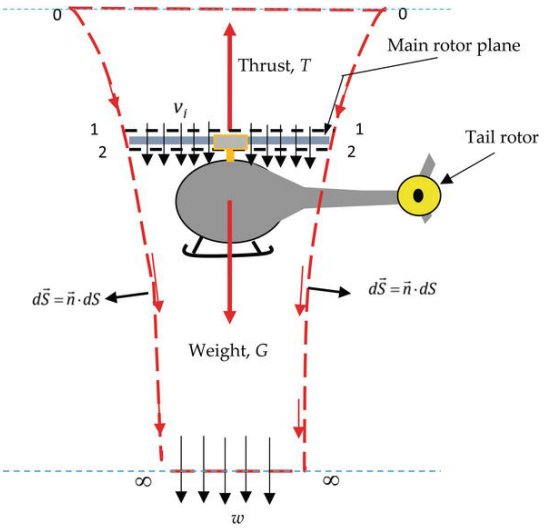

Fig. 9 Momentum-theory flow model for hovering flight[33]

4. Results and Discussion

These results center on two main topics. The first discusses the settling time data. The second topic considers the indirect thermal consequences of running electrical motors at high power settings.

4.1 Transient Response Data

The input and output of a typical transient experiment is presented in Fig. 10. The input is the throttle setting measured by pulse-width modulation (e.g., a pwm value of 1,900 corresponds to 90% throttle). The input is a step function and represented by the red series of lines of Fig. 10. The output is the rotational speed of the rotor motor, represented by the blue lines. The ramp-up is a steep ramp. The coast-down ramp is less steep.

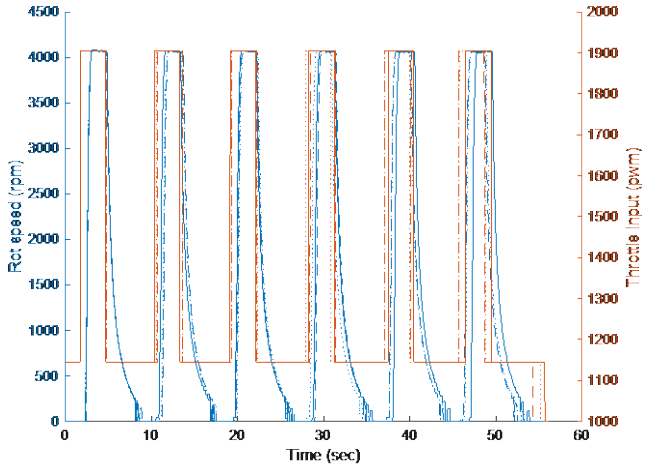

Fig. 10 Typical transient experiment

Figure 10 shows the three different experiments conducted to verify repeatability. These are characterized by a solid line, a dashed line, and a dotted line. As the figure depicts, the results are repeatable. Figure 10 only shows 6 ramp-up and coast-down iterations rather than the 10 discussed in the methodology.

Figure 11 displays the settling time of the different rotor–motor configurations (y-axes) with the change in rotor rpm on the x-axis (left). All data points (approximately 5,000 total) are depicted in these two plots. The left chart in Fig. 11 shows the coast-down transients, and the right chart shows the ramp-up transients. Figure 11 illustrates consistent and similar ramp-up performance by all rotor–motor configurations, so much so that the ramp-up was no longer a consideration in the research.

The coast-down experiments illustrate something altogether different. The settling time behaves differently based upon the configuration. The data points corresponding to the coast-down clearly indicate that the rotor–motor configuration matters, as well as the rotational speed.

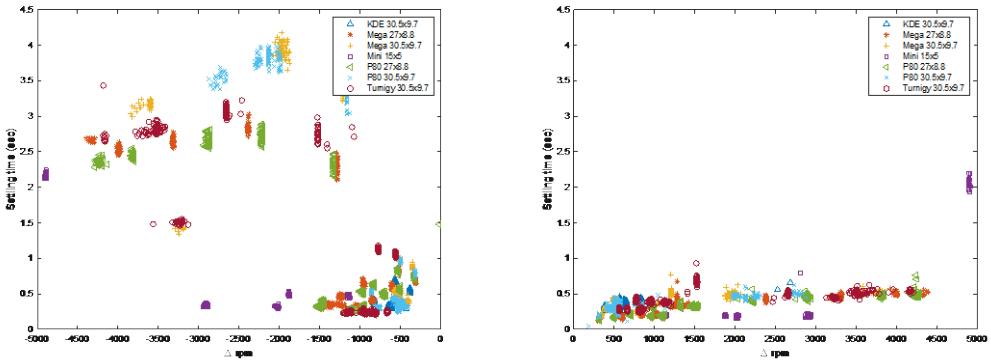

Fig. 11 All transient experiments (left) and ramp-up experiments (right)

Figure 11 also shows more variability in the coast-down response of each rotor–motor configuration than was expected. For example, the coast results of the Mega/KDE 30.5 configuration vary widely based upon the change in rotational speed. The relationship does not strictly increase or decrease. There are some data points with lower speed changes yet with high settling times. Similar behavior appears at higher speed changes. These results are strong indicators of the influence of several variables upon the response, not just the rotor inertia. The variability in these results was initially confusing to the research team until it began to focus on the electric component of the rotor–motor configuration and examine it from the perspective of a brushless DC motor—more specifically the input voltage of the motor. Unlike conventional rotary-wing aircraft that use an overrunning clutch to disengage the rotor from the engine shaft, the electric rotor–motor system remains connected throughout operation. Therefore, the rotor inertia is only one variable affecting the transient time between rotational speeds.

The coast-down conditions are further broken down by voltage and throttle setting. The results are presented in Figs. 12–14 for five of the seven different configurations. The KDE/KDE 30.5 configuration only yielded data for the low-throttle differential settings due to the thermal defects of the two motors. The Mini/TM 15.5 configuration was eliminated because it is a very small-scale configuration with an inertia that is an order of magnitude smaller than the other configurations.

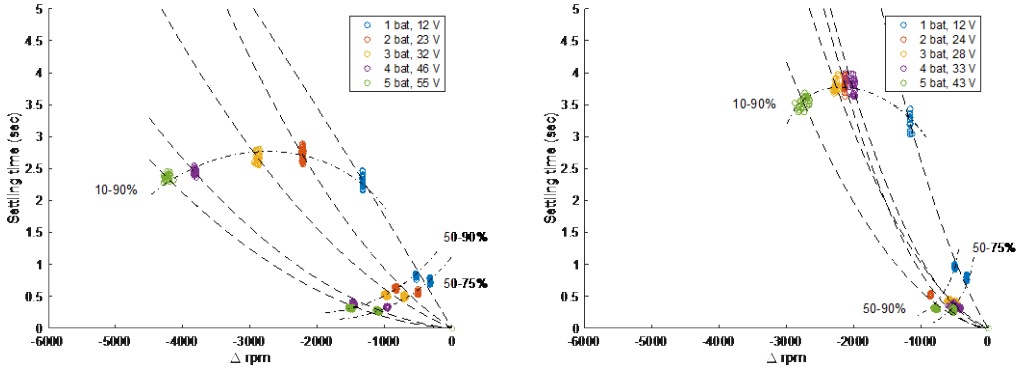

Fig. 12 (left) P80/Falcon 27 and (right) P80/KDE 30.5 voltage and throttle curves

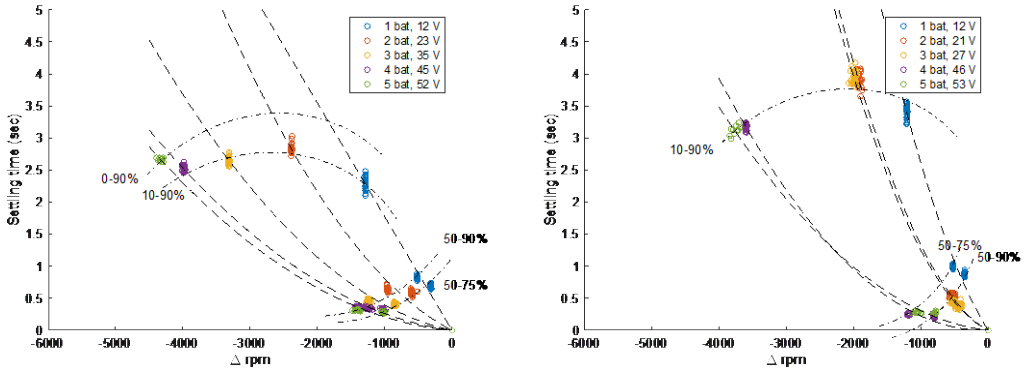

Fig. 13 (left) Mega/Falcon 27 and (right) Mega/KDE 30.5 voltage and throttle curves

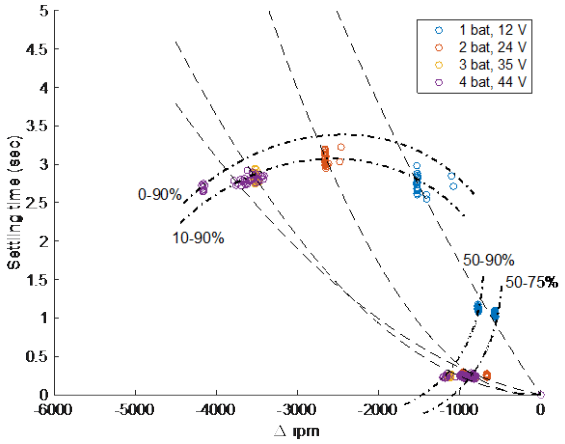

Fig. 14 Turnigy/KDE 30.5 voltage and throttle curves

The data points in Figs. 12–14 are color coded by voltage, which was controlled experimentally by linking automotive batteries in series. The voltage values in the legends are the averages of the voltages measured during the experiments.

The data points are also grouped by two sets of curves. The curves connecting the data points at the same voltage were determined parametrically using the MATLAB Curve-Fit Toolbox. The curves with the percentages represent the data points corresponding to the same throttle differentials during experimentation. The lower differential throttle settings are the 50%–75% and 50%–90% curves, which show low rotational speed changes and low settling times. Based upon the results presented in these charts, the focus of the analysis shifted to the large speed differential settings.

Note the differences in the slope of the curves in Figs. 12–14. The slopes of the voltage curves change as the input voltage changes, although subtly. The throttle curves change more drastically. There is a clear difference in the slopes of the curves at the high throttle differential and the curves of the low throttle differential.

These differing relationships clearly indicate that the transient time is a function of several variables to include the rotational speed, input voltage, and throttle differential.

Figure 13 is the only set of results that show definitively the comparison of rotor inertias on the same motor, the Mega. This observation resulted in the most direct visualization of the change in settling time due to inertia increase. The chart on the left depicts the Falcon 27 rotor, and the chart on the right shows the KDE 30.5 rotor. Increasing the rotor inertia results in the set of curves shifting up and to the right.

Based on the results of Fig. 12–14, the 10%–90% throttle differential data sets were broken down by voltage and configuration. These results are depicted in Fig. 15.

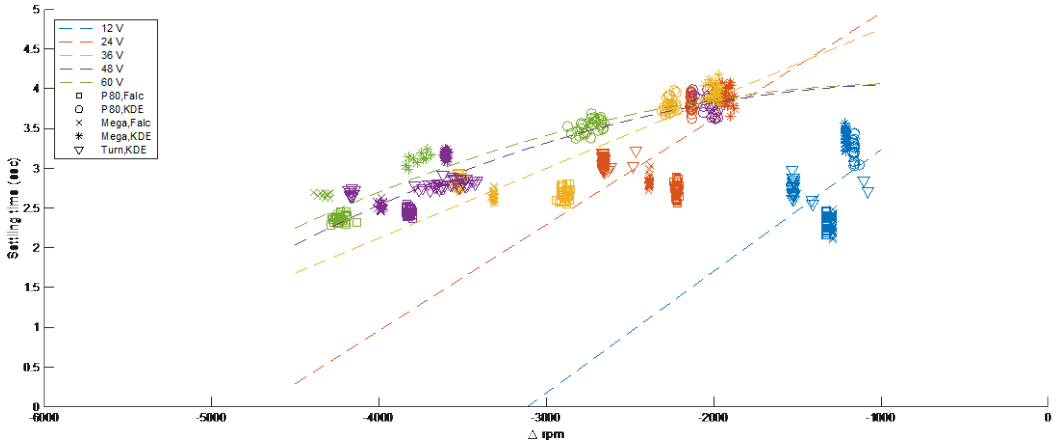

Fig. 15 Settling time of 10%–90% throttle differential categorized by voltage and configuration

The curves in Fig. 15 were generated parametrically, again using MATLAB. These curves show the trends between rotational speed differential and settling time, based upon input voltage. Note how the slope decreases as the voltage increases from 12 to 60 V. Figure 15 also highlights that inertia is not the only contributor to settling time. The Turnigy/KDE 30.5 configuration has the highest inertia of the configurations tested. It is represented by the inverted triangles in the chart. However, it does not have the highest settling times.

Based on these results, it became necessary to look for a multivariable method of capturing the relationship between all the possible input variables and the transient response, which is described in the next section.

4.2 Transient Response Model

The authors originally began investigating the influence of more than 35 input variables on the settling time during the coast phase to incorporate into a stochastic model. Stochastic methods in aerospace applications have been well-documented in the literature.[34–36] However, once the team focused on the electrical motor component, the model became easier to identify.

The differential equations of motion for DC motors are well-defined.[37,38] The electric motors used in UAS applications are 3-phase and require different methods of control,[39] but they are still modeled as brushless DC motors. The differential equations are listed in Eq. 1.

$$\begin{aligned} V(t) &= L_m \dot{I}(t) + R_m I(t) + V_m(t) \\ J\dot{\Omega}(t) &= T_m(t) - B\Omega(t) - Q(t) \end{aligned} \tag{1}$$

and

$$\begin{aligned} T_m(t) &= k_m I(t) \\ V_m(t) &= k_T \Omega(t) \end{aligned} \tag{2}$$

where

B = friction coefficient [N·m/(rad/s)]

I = current (A)

J = rotor–motor inertia (kg.m^2)

L_m = armature inductance (Henries, H)

R_m = armature resistance (ohms, Ω)

Q = load torque (N·m)

T_m = motor torque (N·m)

V = armature (input) voltage (V)

V_m = back emf voltage (V)

k_m = back emf constant (1/kV) [V/(rad/s)]

k_t = torque constant (N·m/A)

Ω = rotational speed (rad/s)

Note that these variables are given in the SI system of units, which are predominant in DC motor analysis. In the SI system, the back emf constant and the torque constants have the same value, although different units. Note that the motor torque is a function of current, and the back emf is a function of rotational speed.

The acceleration is given by

$$\dot{\Omega}(t) = \frac{\Delta\Omega}{\Delta t} \tag{3}$$

Substituting these equations yields an expression for the settling time (Δt):

$$\Delta t = \frac{JR_m\Delta\Omega}{k_t\left(V - L\dot{I} - k_m\Omega\right) - BR_m\Omega - QR_m} \tag{4}$$

Based on the expression in Eq. 4, there are five primary input variables that determine the settling time (Δt): 1) the inertia (J), 2) the change in rotational speed ($\Delta\Omega$), 3) the input voltage (V), 4) the rate of change of the current ($\dot{I}$), and 5) the torque (Q). Rather than use the torque values directly, the absolute value of the change in torque ($|\Delta Q|$) between throttle settings was used. The inductance, resistance, motor constant, torque constant, and friction coefficients are functions of the individual motors used. Only some of these values were known a priori. Many are unknown.

The model was built using the JMP statistical software package. The values of the five input variables and the settling time were extracted from the combined data sets for all rotor–motor configurations. A second-degree factorial, standard least squares model was fit to the data.

The resulting mathematical model consists of 18 terms. The prediction expression output is presented in Fig. 16. Although the variables are represented slightly differently in the JMP software output, they are self-explanatory.

Prediction Expression

-1.456129641
+ 436.48178828 • Inertia
+ -0.00214887 • RPM drop
+ -1.894109815 • Torque change
+ 0.0022752299 • dI/dt
+ (Inertia − 0.0047766277) • ((Inertia − 0.0047766277) • -57537.03442)
+ (Inertia − 0.0047766277) • ((RPM drop − (-1506.287087)) • -0.421183833)
+ (RPM drop − (-1506.287087)) • ((RPM drop − (-1506.287087)) • -3.903684e-8)
+ (Inertia − 0.0047766277) • ((Voltage − 29.301389233) • 7.8289840896)
+ (RPM drop − (-1506.287087)) • ((Voltage − 29.301389233) • -2.581437e-5)
+ (Voltage − 29.301389233) • ((Voltage − 29.301389233) • 0.0007453523)
+ (Inertia − 0.0047766277) • ((Torque change − 1.0127053907) • -191.7271323)
+ (RPM drop − (-1506.287087)) • ((Torque change − 1.0127053907) • 0.0006326499)
+ (Voltage − 29.301389233) • ((Torque change − 1.0127053907) • -0.029211343)
+ (Torque change − 1.0127053907) • ((Torque change − 1.0127053907) • 0.5482948363)
+ (Inertia − 0.0047766277) • ((dI/dt − (-39.46877163)) • 0.7288448535)
+ (RPM drop − (-1506.287087)) • ((dI/dt − (-39.46877163)) • -9.310651e-6)
+ (Voltage − 29.301389233) • ((dI/dt − (-39.46877163)) • -0.000293602)

Fig. 16 Prediction model for settling time (Δt)

The goodness of fit can be evaluated from Fig. 17. As depicted, the model's R-squared value is 0.96. The chart on the left in Fig. 17 shows the actual versus predicted settling time. As the chart shows, in most cases the model captures the relationship very well. The charts on the right show the residual distribution, the upper right by predicted settling time, and the lower right by the row number of the data.

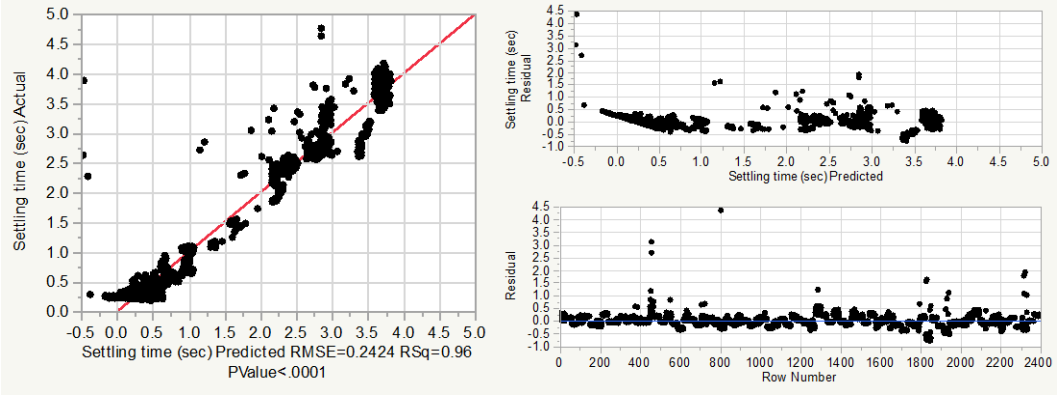

Fig. 17 (left) Model goodness-of-fit and (right) residuals

Note that there are some data points where the model predicts a negative settling time. This is the by-product of a stochastic model but is not problematic since the focus of this model would be on larger-size configurations. Figure 18 displays two profiler windows that allow the user to visualize the influence of each input variable on the response. The upper chart is the P80/Falcon 27 configuration, and the lower chart is the Turnigy/KDE 30.5 configuration. The settling time is on the y-axis. The charts above each input variable represent the settling time as a function of each input variable. Note most of these curves do not have a constant or nearly constant slope. The input variables with steeper slopes have a higher effect on the settling time.

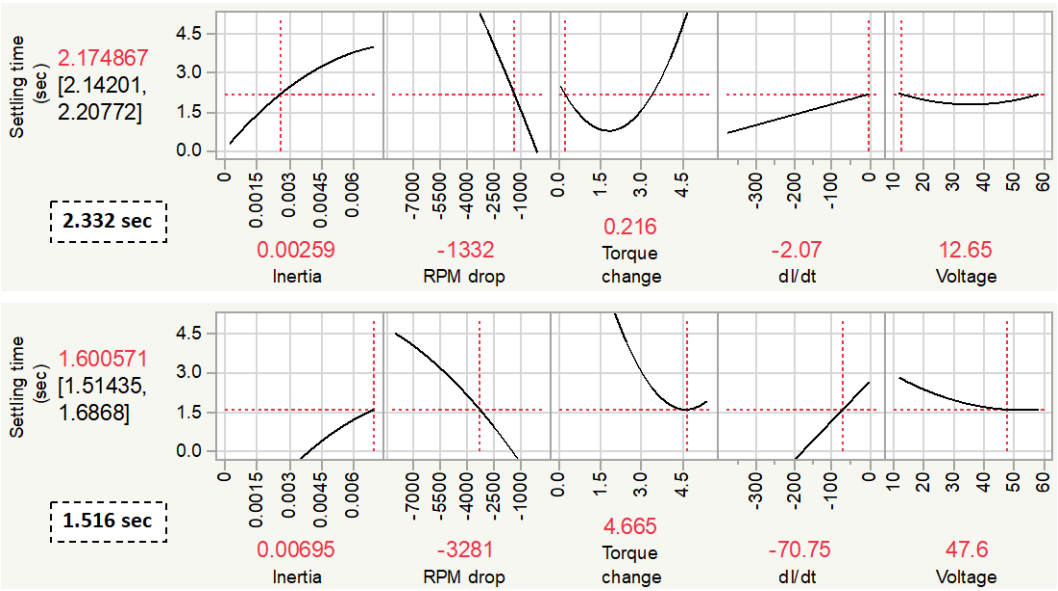

Fig. 18 Prediction model profiler

Note the inertia curves in Fig. 18. As the inertia increases, the slope shallows out, indicating that inertia has less of an effect as the inertia of the rotor increases. The change in rotational speed has the most effect, as does the change in torque.

In the software package, the user can choose the desired value of the input variables, which are given in red below the x-axis. The red value next to the y-axis is the predicted settling time. Below the predicted time is a 95% confidence interval. The boldface numbers in the white dotted boxes are the actual experimental settling times for the input variable conditions. Note that while the actual settling time of the P80/Falcon 27 configuration is outside of the 95% confidence interval predicted by this model, the model is still adequate enough to provide important information regarding the sensitivity of the response to the input variables.

These types of models tend to become less reliable when analyzing the extreme edges of the input variable ranges[36] or extrapolating outside of those ranges. Therefore, more experiments using larger-scale configurations would allow for better, more reliable predictions.

4.3 Thermal Runaway Considerations

During one experiment, the KDE motor began emitting smoke. Upon further investigation, it was determined that the motor had a manufacturing defect. These are depicted in Fig. 19. This meltdown occurred at 4,435 rpm, 3.014 kW, and 24 lbf of thrust, which was well within the operating limits of the motor. It was characterized by a rapid rise in temperature during the experiment and the growing smell of electrical smoke.

Fig. 19 KDE motor overheating during (left) test and (right) postrun damage

This incident brought up an important consideration for running electric motors at high power settings—thermal management. While the rotor–motor is running, the airflow around the motor generally keeps its temperature under control. Once the

airflow generated by the rotor is taken away, the temperature of the motor begins to spike to high and sometimes unsafe temperatures.

After the meltdown incident, more experiments were conducted to study the effects that different test configurations had on the temperature increase at the end of the experiment. The two main experiments used to study thermal considerations were endurance and constant power (while varying voltage and current) experiments. An example of the results of an endurance experiment is shown in Fig. 20. It is clear from the illustration that the temperature levels off while the motor is still spinning, and as soon as the power is removed (and the airflow around the motor stops), the temperature spikes up steeply.

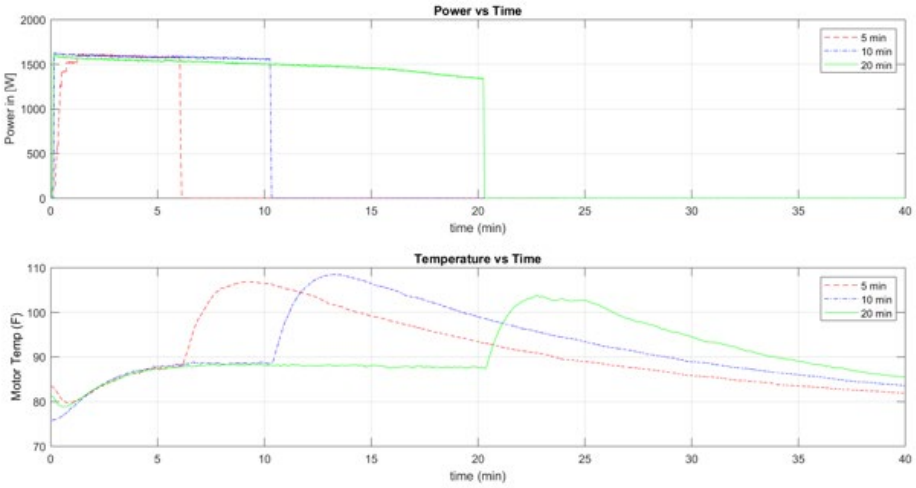

Fig. 20 5-, 10-, and 20-min endurance temperature experiments

Running endurance experiments had its limitations due to the use of automotive batteries as a power supply. Since a constant power source was not used, the larger motors began to draw too much power and drain the batteries during endurance tests. Comparisons for temperature could not be made for larger-motor configurations at a constant power. Therefore, it was not possible to collect a significant number of data for endurance experiments. To properly identify trends, it would be necessary to run future experiments with a constant power source.

The other temperature experiments involved operating a motor at a constant power value for a specified time interval while increasing the input voltage of the system by adding an additional battery in series. Increasing the voltage decreased the current supplied to the system. Nevertheless, the motor still saw an increase in maximum temperature of approximately 1.5° each time there was an increase of approximately 12 V, as shown in Fig. 21. These results were consistent with two other motors included in the experimental runs. Though this experiment was

conducted on three different rotor–motor combinations, more experiments with a variety of motors at different power settings are necessary to verify this trend.

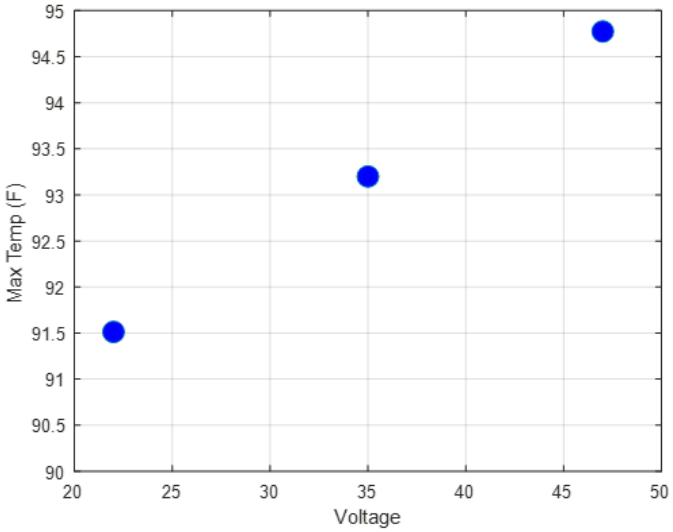

Fig. 21 KDE constant-power (500-W) steady-state temperature experiment

A summary of these experiments is presented in Table 7. All of the experiments consistently show a rapid ride to a peak power within 3.0–3.5 min after the rotor stops with a significant cool-down period afterward. The first three data points in Table 7 are the temperatures depicted in Fig. 21.

Table 7 Thermal experiment summary

Motor (with Falcon 27 rotor)	No. batteries	Power (W)	Run time (min)	Max Temp (°F)	Temp spike time (min)	Temp settling time (min)	Settling temp (°F)
KDE	2	500	5	91.5	3	14	83
KDE	3	500	5	93.2	3.5	5	89
KDE	4	500	5	94.8	3	18	82
P80	2	300	5	86	3	17	80
P80	3	300	5	88.4	3.5	20	80
P80	4	300	5	90.6	3	23	80
P80	3	800	5	94.3	3	15	84
P80	4	1.6 K	5	106.9	3	39	80
P80	4	1.6 K	10	108.5	3	31.5	82
P80	4	1.57 K	20	103.8	3	32	80

The thermal considerations are important because of the high power requirements of VTOL aircraft. As initially presented in Table 1, the nominal Group III UAS aircraft requires a hover power of approximately 60 hp (45 kW). This is well above the maximum power of 1.57 kW presented in Table 7.

A VTOL aircraft landing from a hover completes its flight at one of the highest power conditions in the flight envelope. This leads to one of the highest temperature conditions of an electric motor. For a conventional Army helicopter, this is followed by a 20-minute period at idle to allow the powerplant to begin its cool-down. Currently, sUAS rotors stop immediately upon landing to prevent a rollover, resulting in the immediate loss of cooling.

For quadcopter-type configurations to scale to larger platforms, a thermal strategy must be developed. Strategies could incorporate a cool-down period at low-power setting to continue the airflow. It could also include electric motors that are cooled by means other than air, such as water or water glycol.[40] Understanding the effects of sustained heat on electric motors at high-power settings must be further studied.

4.4 Regenerative Braking Studies

Some electronic speed controllers have the capability to provide regenerative braking (RB) to return power to the batteries. A quick set of experiments using the Mega/Falcon 27 and Mega/KDE 30.5 configurations was run to determine if there were any distinguishable effects of having the RB feature on or off. These results are presented in Fig. 22. In this set of experiments, there was no discernable difference in the settling time between RB settings. However, more experiments are required to adequately explore the effects of RB.

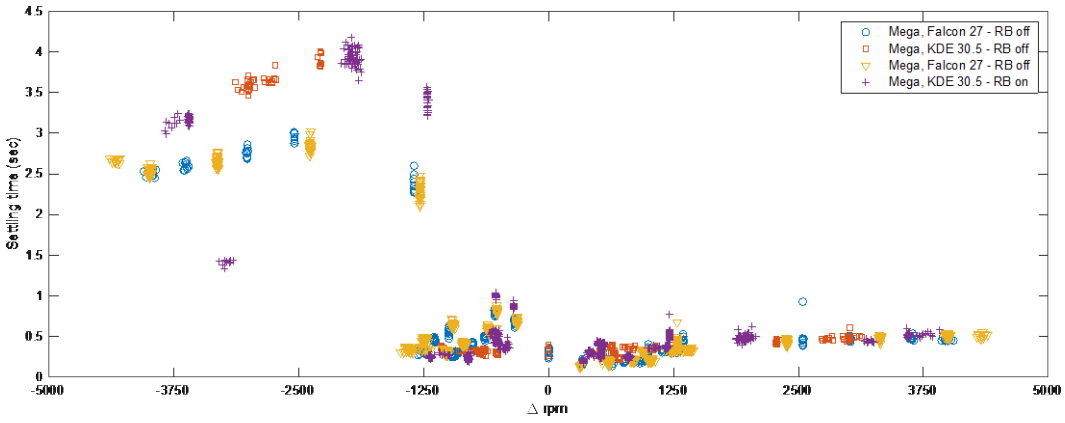

Fig. 22 Mega motor configurations RB comparisons

5. Comparison with Other Rotary-Wing Platforms

The authors also captured data to compare the different rotor–motor configurations with conventional aircraft. Figure 23 depicts the power coefficient versus thrust coefficient for a variety of platforms. The rotor–motor configurations used in this study have been added to compare with existing platforms. The data points were calculated using Eq. 4. The curve labelled "curve-fit" represents a curve-fit of the data points using MATLAB. The ideal curve represents the ideal conditions of basic momentum theory. In Fig. 23 most of the electric motors, with the exception of one, are on the higher end of the chart. Conventional VTOL aircraft fall on the lower end of the chart.

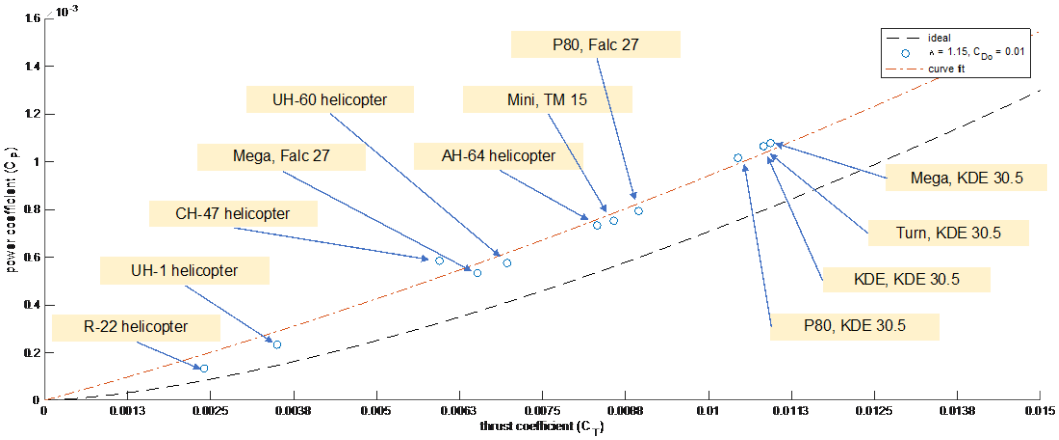

Fig. 23 Thrust–power comparisons with VTOL platforms

Leishman's text on helicopter aerodynamics[33] provides an overview of the relationship between the disk loading of VTOL aircraft and hovering efficiency, defined as power loading, which is the power per unit weight of the aircraft. In addition to Leishman's original data points, conventional Army helicopters as well as the rotor–motor combinations used in this study have been added. These results are presented in Fig. 24.

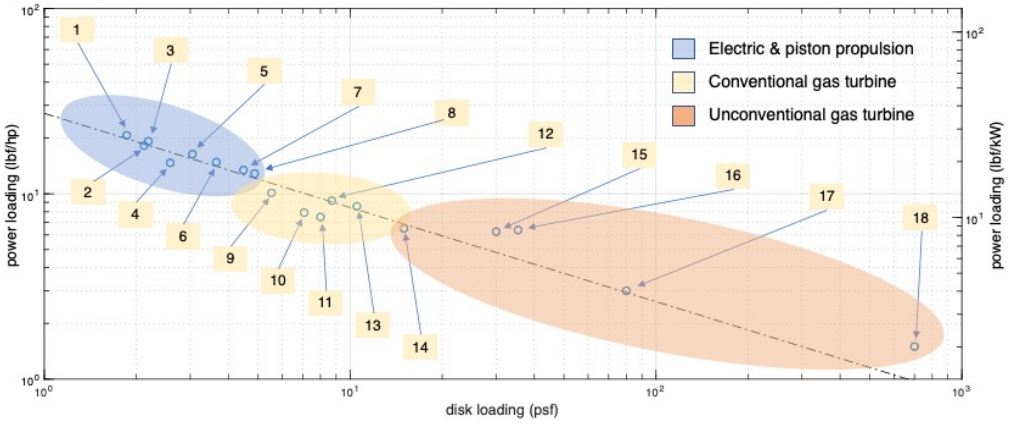

1: P80/KDE 30.5
2: Mega/Falc 27
3: KDE/KDE 30.5
4: R-22 helicopter
5: P80/Falc 27
6: Mini/TM 15
7: Mega/KDE 30.5
8: Turn/KDE 30.5
9: UH-1 helicopter
10: CH-47 helicopter
11: Pure helicopter
12: UH-60 helicopter
13: AH-64 helicopter
14: Compound helicopter
15: Tilt-rotor
16: Nominal group III UAS
17: Tilt-wing
18: Vectored thrust

Fig. 24 Hovering efficiency (power loading) vs. disk loading comparison

The data in Fig. 24 show three distinct regions of the chart, highlighted by the three different shaded areas. The first region, shaded in blue, contains all the rotor–motor combinations as well as the R-22 helicopter, which uses an internal combustion (piston) engine. The second shaded region includes the conventional VTOL gas-turbine helicopters. Unconventional gas-turbine configurations are represented by the third area, shaded in red. Note the secondary axis contains nonstandard units (foot pounds per kilowatt). These combine the weight units of the US helicopter and the power output of the electric motor.

Figure 24 seems to indicate that these smaller electric propulsion elements have higher hovering efficiency than their larger counterparts. Much more analysis of larger electric motors is necessary before drawing any definitive conclusions.

6. Conclusions

This report details the results of a study designed to study the scalability of sUAS rotor–motor configurations for heavier platforms, particularly with respect to the transient results. A summary of the significant conclusions follows:

- The rotational speed coast-down transient settling time is more sensitive to inertia than the ramp-up transient settling time.

- Inertia is only one component that affects the settling time of the rotor–motor configuration. Other significant factors include voltage, torque change, rotational speed change, and the time rate of change of the current.
- A model was generated from the experimental data to predict the settling time as a function of these input variables.
- Temperature and thermal management are critical considerations for variable-speed motors.
- The data and operation of these rotor–motor configurations conform to conventional rotary-wing aerodynamic theory and can be analyzed as such.
- More experiments are required to expand the data sets available for making predictions.

7. Recommendations for Further Research

7.1 Further Investigate the Driving Physical Forces behind the Transient Response of Variable-Speed Configurations

Several questions still exist based upon the results of this study. While it was demonstrated that inertia does affect the settling time of the rotor–motor configuration, other factors were established as equally important. The size/scale limits of variable-speed rotors were not discovered. More experiments are required to fully understand the combined effects of inertia and profile drag. The effects of RB through electronic speed control were not fully explored. Finally, the model shows that the influence of the input parameters changes depending upon their values, which is very different from the mechanical linkage of a powerplant, transmission, and rotor of a conventional rotary-wing aircraft. The physics, dynamics, and intricacies of electric UAS motors, such as timing, resistance, control, and the like need to be better understood by the rotary-wing community.

7.2 Investigate Scalability of Quadcopter Configurations Using Much Larger-Scale Rotor–Motor Configurations than the Previous Study

The only way to determine the true scalability of quadcopter-type configurations in the Group III UAS regime is to experiment with full-scale or near-full-scale rotor–motor combinations. The proposed test stand provides the capability to conduct this type of research activity.

7.3 Investigate the Thermal Properties of Electric Motors under Peak and Nonpeak Performance Demands and Their Effects on Motor Durability

Prolonged operation at high power settings can change the properties and performance of electric motors over time. These types of research activities will allow for the thermal characterization of different motors and perhaps generate some thermal mitigation strategies and procedures.

7.4 Other Research Activities

In addition to these activities, other useful follow-on research topics include the following:

- Investigate the feasibility of using rotors produced by additive means.
- Investigate the performance, damage tolerance, and endurance of mid-to-full-size rotor systems manufactured conventionally or additively.
- Investigate the short- and long-term performance of rotor–motor configurations using different means of system power (battery, electric constant power, conventional hydrocarbon, fuel cell, etc.).
- Investigate the feasibility of new rotor-hub mechanisms for both UAS and helicopter applications.

These research activities require a large-scale VTOL propulsion test stand on the order of 125 kW to continue this research. The specifications of such a test stand are presented in Table 8. Such a test stand can simulate aircraft between 640 lb (30 kW) and 3,300 lb (125 kW).

Table 8 125-kW large-scale test stand nominal specifications

Max continuous power	125 kW
Max rotor diameter	72 inches
Max rotational speed (72-inch-diameter rotor)	2,842 rpm
Max rotational speed (30-inch-diameter rotor)	6,820 rpm
Max thrust load	825 lb
Max torque	310 ft-lb

8. References

1. Schroth L, Bodecker H, Radovic M. The drone market report 2019: the commercial drone market size and forecast 2019–2024. DRONEII.com; 2019 Mar [accessed 2019 Sep 19]. https://www.droneii.com/project/drone-market-report.

2. Federal Aviation Administration. Small unmanned aircraft systems [accessed 2017 June 28]. https://www.ecfr.gov/cgi-bin/text-idx?SID=0cb4bf8c80615851b712c2f4a9a289a9&mc=true&node=pt14.2.107&rgn=div5#sp14.2.107.a.

3. Lang K. Amazon's plea to feds: let drones deliver. The Hill; 2015 Apr.

4. Amazon Prime Air; 2017 [accessed 2017 June 28]. https://www.amazon.com/Amazon-Prime-Air/b?node=8037720011.

5. US Department of Defense. Unmanned systems integrated roadmap: 2013–2038. Washington (DC): Department of Defense (US); 2013. Open Publication Reference No.: 14-S-0553.

6. Klein D. Fiscal 2020 defense budget request includes billions for unmanned systems. Unmanned Systems Magazine; 2019 June 24 [accessed 2020 May 4]. https://www.auvsi.org/unmanned-systems-magazine-fiscal-2020-defense-budget-request-includes-billions-unmanned-systems.

7. Carey N. UPS-backed Rwandan blood deliveries show drones' promise, hurdles. Reuters; 2016 May.

8. Cutler M, Ure NK, Michini B, How JP. Comparison of fixed and variable pitch actuators for agile quadrotors. Proceedings of the AIAA Guidance, Navigation, and Control Conference; 2011. p. 1–17.

9. Weatherington DD. Post Iraq and Afghanistan: current and future roles for UAS and the fiscal year 2014 budget request, testimony before the House Armed Services Committee; 2013 Apr 23 [accessed 2019 Sep 19]. https://www.govinfo.gov/content/pkg/CHRG-113hhrg80763/html/CHRG-113hhrg80763.htm.

10. Holden J, Goel N. Fast-forwarding to a future of on-demand urban air transportation. Uber Elevate. 2016 Oct. https://www.govinfo.gov/content/pkg/CHRG-113hhrg80763/html/CHRG-113hhrg80763.htm.

11. Bouabdallah S, Siegwart R. Towards intelligent miniature flying robots. In: Corke P, Sukkarieh S, editors. Field and service robotics: results of the 5th international conference; 2006. Berlin (Germany): Springer; c2006. p. 429–440.

12. Davis TL. Development and characterization of a UAS propulsion test bench [master's thesis]. [Kent (OH)]: Kent State University; 2018.

13. Alexis K, Nikolakopoulos G, Tzes A. Switching model predictive attitude control for a quadrotor helicopter subject to atmospheric disturbances. Control Eng Pract. 2011;19(10):1195–1207.

14. Basri MAM, Husain AR, Danapalasingam KA. Enhanced backstepping controller design with application to autonomous quadrotor unmanned aerial vehicle. J Intell Robot Syst Theory Appl. 2015;79(2):295–321.

15. Czyba R. Design of attitude control system for an UAV-type quadrotor based on dynamic contraction method. Proceedings of the IEEE/ASME International Conference on Advanced Intelligent Mechatronics; 2009; Singapore. p. 644–649.

16. Nicol C, Macnab CJB, Ramirez-Serrano A. Robust neural network control of a quadrotor helicopter. Proceedings of the Canadian Conference on Electrical and Computer Engineering; 2008 May. p. 1233–1238.

17. Ouassaid M, Cherkaoui M, Zidani Y. A nonlinear speed control for a Pm synchronous motor using an adaptive backstepping control approach. Proceedings of the IEEE International Conference on Industrial Technology; 2004. Vol. 3. p. 1287–1292.

18. Wang W, Yuan X, Zhu J. Automatic Pid tuning via differential evolution for quadrotor UAVs trajectory tracking. Proceedings of the IEEE Symposium Series on Computational Intelligence; 2016; p. 1–8.

19. Driessens S, Pounds P. The triangular quadrotor: a more efficient quadrotor configuration. IEEE Trans Robot. 2015;31(6):1517–1526.

20. Driessens S, Pounds PEI. Towards a more efficient quadrotor configuration. Proceedings of the IEEE/RSJ International Conference Intelligent Robots and Systems; 2013. p. 1386–1392.

21. Pounds P, Mahony R. Design principles of large quadrotors for practical applications. Proceedings of the IEEE International Conference on Robotics and Automation; 2009 May. p. 3265–3270.

22. Famouri P. Control of a linear permanent magnet brushless DC motor via exact linearization methods. IEEE Trans Energy Convers. 1992;7(3).

23. Kader SA, El-henawy A, Oda AN. Quadcopter system modeling and autopilot synthesis. Int J Res Technol. 2014;3(11):9–14.

24. Tayebi A, Mcgilvray S. Attitude stabilization of a four-rotor aerial robot. Proceedings of the 43rd IEEE Conference on Decision and Control; 2004 Dec.

25. Wang P, Man Z, Cao Z, Zheng J, Zhao Y. Dynamics modelling and linear control of quadcopter. Proceedings of the IEEE International Conference on Advanced Mechatronic Systems; 2016; p. 498–503.

26. Sepe RB, Lang JH. Real-time observer-based (adaptive) control of a permanent-magnet synchronous motor without mechanical sensors. IEEE Trans Ind Appl. 1992;28:1345–1352.

27. Petrović V, Ortega R, Stanković AM. Interconnection and damping assignment approach to control of Pm synchronous motors. IEEE Trans Contr Syst Technol. 2001;9(6):811–820.

28. Heng L, Meier L, Tanskanen P, Fraundorfer F, Pollefeys M. Autonomous obstacle avoidance and maneuvering on a vision-guided MAV using on-board processing. Proceedings of the IEEE International Conference on Robotics and Automation; 2011 May. p. 2472–2477.

29. Dai M, Keyhani A, Sebastian T. Fault analysis of a PM brushless DC motor using finite element method. IEEE Trans Energy Convers. 2005;20(1):1–6.

30. Sekhar AS, Prabhu BS. Condition monitoring of cracked rotors through transient response. Mech Mach Theory. 1998;33(8):1167–1175.

31. Stringer DB, Edmonds K. Unmanned VTOL propulsion: scalability of quadcopter rotor-motor configurations outside the small UAS regime. Presented at the US Army Research Laboratory Vertical-Takeoff-and-Landing Propulsion Workshop; 2018 Dec 12; Aberdeen Proving Ground, MD.

32. RC Benchmark. Tools for UAV designers [accessed 2019 Mar 26]. www.rcbenchmark.com.

33. Constantin R, Todorov M. Helicopter flight physics – models, techniques and technologies. London (England): IntechOpen; 2017 Dec 20. [accessed 2020 Apr 22]. https://www.intechopen.com/books/flight-physics-models-techniques-and-technologies/helicopter-flight-physics.

34. Mavris DN, DeLaurentis DA. A probabilistic approach for examining aircraft concept feasibility and viability. Aircr Des. 2000;3(2):79–101.

35. Mavris D, DeLaurentis D, Bandte O, Hale M. A stochastic approach to multi-disciplinary aircraft analysis and design. Proceedings of the AIAA 36th Aerospace Science Meeting and Exhibition; 1998. p. 1–17.

36. Stringer DB, Bunner DW, Winkler RW. Aerospace capstone design: interactive initial sizing estimates for increasing designer intuition and mitigating risk in the early stages of aircraft conceptual design. Presented at the American Society for Engineering Education Annual Conference and Exposition; 2018.

37. Ogata K. System dynamics. Vol. 3. Upper Saddle River (NJ): Prentice Hall; 1998.

38. Pal D. Modeling, analysis and design of a DC motor based on state space approach. Int J Eng Res Tech. 2016;5(02):293–296.

39. Harrington AM, Kroninger C. Characterization of small DC brushed and brushless motors. Fort Belvoir (VA): Defense Technical Information Center; 2013 Mar.

40. EMRAX 228. EMRAX innovative motors [accessed 2019 May 12]. https://emrax.com/products/emrax-228/.

Appendix. Rotary-Wing Parameter Calculations

The following equations govern the calculation of standard rotary-wing parameters.

Thrust coefficient: $$C_T = \frac{T}{\rho A(\Omega R)^2} \tag{A-1}$$

Power coefficient: $$C_P = \frac{P}{\rho A(\Omega R)^3} \tag{A-2}$$

From basic momentum theory, the ideal power coefficient is given by

$$C_P = \frac{C_T^{3/2}}{\sqrt{2}} \tag{A-3}$$

Eq. A-3 is defined as the induced power.

The actual power coefficient is the sum of the induced power, corrected for non-ideal conditions, and the profile power. The induced power correction, κ, is often assumed to be 1.15. The profile power is the power required to rotate the rotor blades around the mast.

$$\begin{aligned} C_P &= C_{P_i} + C_{P_o} \\ C_P &= \frac{\kappa C_T^{3/2}}{\sqrt{2}} + \frac{1}{8}\sigma C_{D_o} \end{aligned} \tag{A-4}$$

where

A = disk area (ft^2)

I = current (A)

P = power (ft.lbf/s, hp, W)

R = blade radius (ft)

T = thrust (lbf)

κ = induced power correction factor ~1.15 (dimensionless)

ρ = air density ($slug/ft^3$)

σ = solidity ratio (dimensionless)

Ω = rotational speed (rad/s)

List of Symbols, Abbreviations, and Acronyms

Δt	settling time
Ω	rotational speed
a_{max}	maximum acceleration
d'less	dimensionless
DC	direct current
ESC	electronic speed controller
FY	fiscal year
MSL	mean sea level
η	mechanical efficiency
P_{in}	electrical power in
P_{out}	mechanical power out
pwm	pulse-width modulation
Q	torque
RB	regenerative braking
SI	International System of Units
slug	unit of mass
sUAS	small unmanned aircraft system
T	thrust
UAS	unmanned aircraft system
UK	United Kingdom
VTOL	vertical take-off and landing

1 (PDF)	DEFENSE TECHNICAL INFORMATION CTR DTIC OCA
1 (PDF)	CCDC ARL FCDD RLD CL TECH LIB
1 (PDF)	CCDC ARL FCDD RLV P M RIGGS